Impact of rupture complexity on seismic hazard: Case of the 2018 M_w7.5 Palu earthquake

Liqing Jiao[1,2], Teng Wang[3], Guangcai Feng[4], Paul Tapponnier[5], Andrean V. H. Simanjuntak[6], Chung-Han Chan[7,8*]

5 [1]SinoProbe Center, Chinese Academy of Geological Sciences, Beijing, China
[2]Institute of Geology, Chinese Academy of Geological Sciences, Beijing, China
[3]School of Earth and Space Sciences, Peking University, Beijing, China
[4]Department of Geomatics, Central South University, Changsha, China
[5]National Institute of Natural Hazards, Beijing, China
10 [6]Meteorology, Climatology and Geophysical Agency of Indonesia, Jakarta, Indonesia
[7]Department of Earth Sciences, National Central University, Taoyuan, Taiwan
[8]Earthquake-Disaster & Risk Evaluation and Management (E-DREaM) Center, National Central University, Taoyuan, Taiwan

Correspondence to: Chung-Han Chan (hantijun@googlemail.com)

Abstract. Rupture complexity results in difficulty with quantifying seismic hazards, such as the probability of an earthquake
15 on multiple segments in an active fault system and spatial distribution of the fault displacement on the surface. Here we propose
a dynamic model to explain rupture complexity. To confirm this model's credibility, we used it to explain the rupture behavior
of the 2018 M_w7.5 Palu earthquake, which splayed along several sub-fault planes on the surface. The Palu event initiated on
an unidentified fault and propagated on a curved plane on the Palu-Koro and Matano faults. According to the Interferometric
Synthetic Aperture Radar data, both principal (on-fault) and distributed (off-fault) faulting were identified, and spatial
20 displacement on the surface could be evaluated. To model the complex geometry of the coseismic rupture plane and
corresponding deformation, we proposed a dynamic model through the discrete element method. Our model demonstrated
rupture along a planar fault at depth and several splay faultings with various deformation on the surface, corresponding to the
observations. The simulations represented temporal rupture behavior that covers several earthquake cycles and probability of
superficial fault displacement that shed light on subsequent seismic hazard assessment and probabilistic fault displacement
25 hazard analysis, respectively.

1 Introduction

Understanding the detailed rupture geometry of a single earthquake is crucial for assessing the seismic hazard in respect to
estimating potential maximum earthquake magnitudes, forecasting probability of an earthquake on multiple fault segments,
and evaluating spatial distribution of fault displacement on the surface. Superficial fault complexity was observed in several
30 recent earthquake cases. These include, the 2001 M_w 7.8 Kokoxili, China, earthquake (Klinger et al., 2005; Xu et al., 2002);
the 2002 M_w 7.9 Denali, US, earthquake (Dreger et al., 2004); the 2016 M_w 7.8 Kaikōura, New Zealand, earthquake (Hamling
et al., 2017); and the 2018 M_w 7.5 Palu, Indonesia, earthquake (Bao et al., 2019; Socquet et al., 2019; Ulrich et al., 2019). Their

rupture lengths appear to be mainly controlled by stress concentrations or stress shadows, and by a fault's geometrical complexities on the surface (Perrin et al., 2016; Wesnousky, 2006, 2008). Knowing how ruptures propagate at depth and on
35   which fault planes is critical for estimating the sizes/geometries of seismic faults, and hence the potential areas most affected by single earthquakes.

The complex rupture behavior could result in difficulty applying rupture dimension and recurrence interval to the seismic hazard assessment. Traditionally, a probabilistic seismic hazard assessment (e.g., Cornell, 1968) assumes an earthquake occurs on an identified active fault. The procedures of these approaches, however, do not fulfill the cases with complex rupture
40   geometry, an earthquake that takes place on multiple active faults. Thus, some innovative approaches (e.g., Chang et al., 2022) have assumed an earthquake could rupture along multiple fault segments. Based on this approach, it is crucial to comprehend the mechanism to determine whether two fault systems could rupture in a coseismic period.

Superficial fault complexity could also lead to a challenge for a probabilistic fault displacement hazard analysis (e.g., Youngs et al., 2003). When a fault is close to a site of interest, an earthquake on the fault might not only generate ground shaking, but
45   also result in fault displacement. Some previous studies (e.g., Peterson et al., 2011; Takao et al., 2013; Youngs et al., 2003) have proposed conditional probabilities of secondary faults as a function of distance to the main fault trace by regression from observations. However, due to limited observations on rupture traces, it is desired to propose an alternative way to sum up distribution of surface fault traces.

Thus, we propose a dynamic model to explain complex rupture behavior. To evaluate this model's credibility, we simulated
50   the rupture behavior of the Palu earthquake. We first identified the seismicity activity in the earthquake's surrounding region according to observations. We then analyzed dislocations along the fault traces and surface displacement according to the Interferometric Synthetic Aperture Radar (InSAR) data. To explain the observations, we implemented the discrete element method (DEM) to simulate the dynamic procedure of fault generation. To demonstrate this model's feasibility, we forecasted earthquake cycles and quantified spatial distribution of secondary faults. The outcomes would be beneficial to subsequent
55   seismic hazard assessment and probabilistic fault displacement hazard analysis.

2 Sulawesi and rupture behavior of the Palu earthquake

2.1 Tectonic setting for Sulawesi

The 2018 M_w7.5 Palu earthquake caused a tsunami and massive liquefaction around the Palu region in central Sulawesi (Oral et al., 2020). This event struck the western edge of the convergent Pacific-Australian-Eurasian triple junction (Fig. 1a). Relative
60   to the Sunda plate, the west-northwestward convergence rate of the Pacific plate is ca. 110 mm per year (Socquet et al., 2006), among the fastest in the world. To the southwest, the Australian plate subducts north-northeastward beneath the Eurasia plate with a rate of ca. 70 mm per year. The complex deformation at north and south Sulawesi results from the combination of these orthogonal boundary motions. Northeast Sulawesi (the Sula Block) thus moves ca. 42 mm per year to the NNW relative to

Borneo and rotates clockwise by ca. 2.5 degrees per million years from the GPS observations shown in Fig. 1 (Socquet et al.,
65   2006). To the south of the city of Palu, the 1909 event ruptured along the Saluki segment; the 1968 event ruptured along the
Moa segment; the 2009 event ruptured along the Palu segment of the Palu-Koro fault, and the 2012 event ruptured along the
branch segment toward Lake Lindu (Fig. 1a; Daryono, 2016). The topography shows the 2018 Palu event ruptured along the
boundaries between the mountain and basin (Fig. 1b). The geological structure of this formation implies that the fault between
the mountain and basin tends to dip toward the basin in different directions.

70
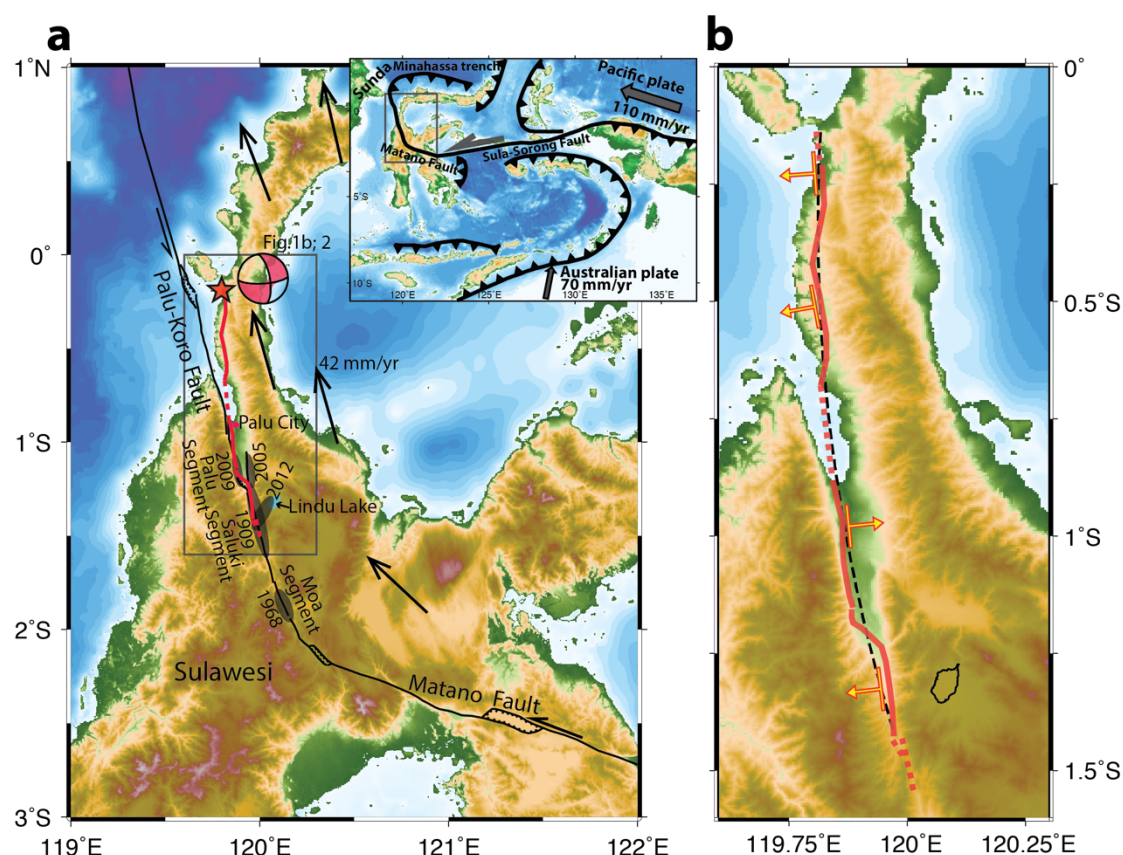
**Figure 1: Tectonic settings and pre-existing faults in the Palu zone: (a) pre-existing faults and previous ruptures from south to north:
the 1968 rupture along the Moa segment, the 1909 rupture along the Saluki segment, the 2009 rupture along the Palu segment of the
Palu-Koro Fault, and the 2012 rupture along a branch. Black arrows show the tectonic movements observed by GPS, showing the**
75   **left-lateral strike-slip moving along the Matano and Palu-Koro faults. The red star shows the epicenter of the 2018 M_w7.5 earthquake.
The red lines show the rupture alignments of the 2018 Palu event. The rectangle zone has more observations from the 2018 event in
(b) and Fig. 2. Inset map: tectonic settings of the Palu zone: triple convergent junction zone, relative to Sunda-Asain, ca. 110 mm/year
convergent rate of the Philippine-Pacific plate toward the northwest, and ca. 70 mm/year convergent rate of the Australian plate
toward the northeast; (b) dip directions along fault segments are suggested by the topography.**

80

2.2 Rupture behavior of the Palu earthquake

The Palu earthquake ruptured 177 km on multiple segments along the fault system (Natawidjaja et al., 2021). It initiated at ca. 70 km north of the city of Palu (Fig. 1) at a shallow depth of 20 km. This earthquake likely occurred due to a slip on the fast slipping, predominantly SSE-trending strike-slip faulting. When the rupture propagated to the south of Palu and reached the

85 east-dipping pre-existing Palu-Koro fault, the event resulted in NS-trending, predominantly left-lateral faulting, with a surface slip of up to ca. 6 m along a series of segmented faults (Bao et al., 2019; Socquet et al., 2019). The sentinel optical and the Synthetic Aperture Radar data highlight multi-segment faulting during this event (Bacques et al., 2020; Fang et al., 2019). North of Palu, the surface fault traces (possibly immature) (Manighetti et al., 2007; Perrin et al., 2016) were previously unmapped or considered inactive (Watkinson & Hall, 2017). South of Palu, the earthquake ruptured along the well-known,

90 left-lateral Palu-Koro fault with a geodetic slip rate of 40 mm per year (Socquet et al., 2006). These faults belong to two distinct systems with strikingly different tectonic/mechanic characters. To the north, the ca. 120 km-long fault system with westward step-overs that cuts across modestly west-dipping hill slopes was never identified. To the south, the ca. 60 km-long, morphologically spectacular, mature fault with eastward step-overs bounds the steeply east-facing slope of a mountain range that rises above 2,000 m. The westward to eastward step-over shift implies that seismic faulting did not occur on a simple

95 uniformly dipping plane (Fig. 1b).

The strongly curved geometry of the Matano/Palu-Koro fault reflects such kinematics and rotation, which suggests that the 2018 rupture also followed a curved, convex to the west, path at depth. On the other hand, recent studies have confirmed that the rupture speed of this event reaches shear wave velocity (known as 'supershear'; Bao et al., 2019; Socquet et al., 2019), suggesting rupture along a fault plane at depth (Burridge, 1973). Okuwaki et al. (2020) also confirmed that this complex fault

100 system has potential for supershear rupture and proposed the peculiar inchworm-like slip evolution. These evidences strongly infer that this event should rupture on multiple segments along one fault system, probably at the seismogenic depth, splay several sub-faults along the sub-fault planes on the way to propagate upward, and form segments on the surface (Jiao et al., 2021; Klinger, 2010; Lefevre et al., 2020).

3 Coseismic rupture analysis at the surface based on the InSAR data

105 To understand detailed superficial rupture behavior and surface displacement, we assessed the InSAR data from the Advanced Land Observing Sattellite-2 (ALOS-2). The principal (shown as red lines in Fig. 2a and black lines in Fig. 2c) and distributed (shown as white lines in Fig. 2c) faulting of the 2018 rupture exhibit bow-shape surface ruptures, concave to the east, from north to south, with ca. 5 segments S1-5 from north to south (Fig. 2a). The earthquake ruptured for a total length of ca. 160 km. The analyzed coseismic displacement (Fig. 2b) along the fault showed peak displacement at the segment along S4 (5.0 m

110 and 6.5 m along profiles P4 and P5, respectively) on the pre-existing Palu-Koro fault. Whereas, less slip along segments S1

and S2 (2.0 and 3.0 m along profiles P1 and P2, respectively) may account for an unmapped fault. Little InSAR data are available along segment S3 that crosses the water area of Palu Bay. Few significant events took place according to the recorded two-year pre- and after-shocks (05 Jan. 2018 to 30 Dec. 2019) between S3 and S4 in the Palu basin (Fig. 2a), which might account for the pre-existing fault segments. A relatively smaller coseismic rupture along S5 (3.5 m and 3.0 m along profiles

115 P6 and P7, respectively) can be explained by the connected eastward stepover toward the end of the rupture. The horizontal deformation from the InSAR data implies the different dip directions along the different rupture segments (vectors in Fig 2d). From north to south, the InSAR observations at the vertical component suggest the S1 slightly west dipping, the S2 and S3 mostly vertical, the S4 east dipping and the S5 west dipping again (color scales in Fig. 2d).

120
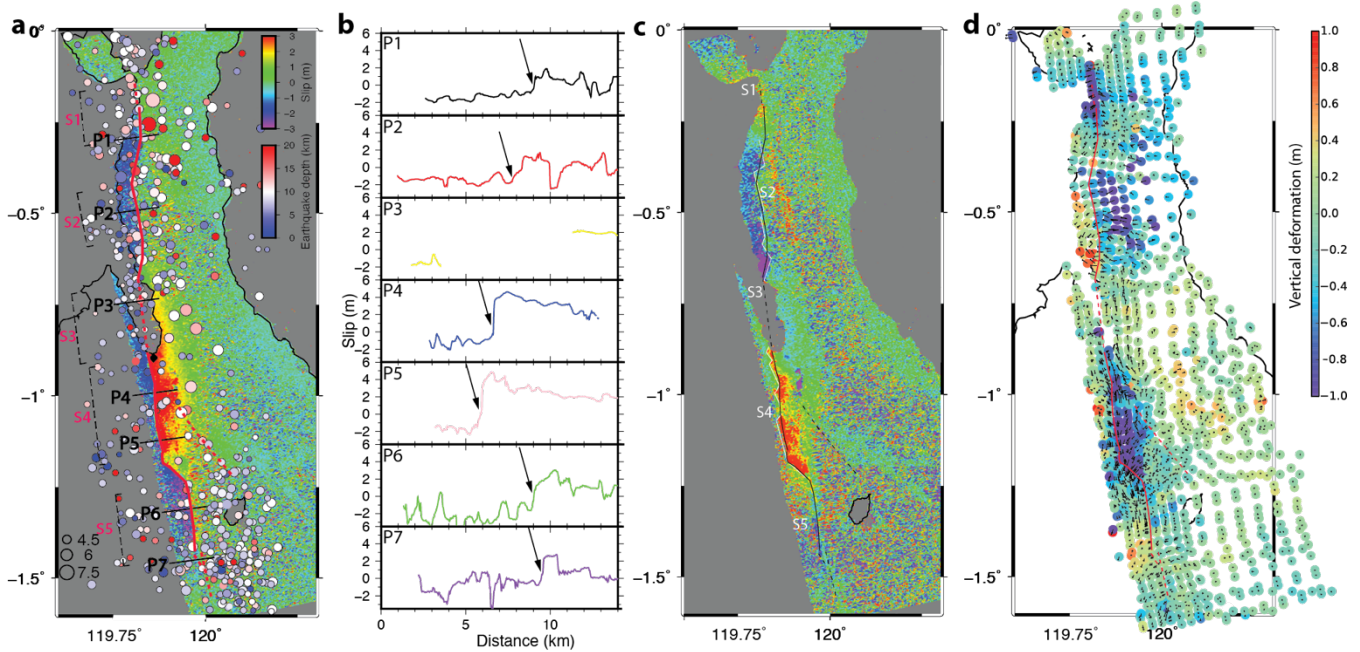
Figure 2: Deformation of the Sulawesi zone by the 2018 Palu event from InSAR and seismic data: (a) InSAR data from ALOS-2 show slip deformation along the N-S direction. The colored dots, whose size and color vary with magnitude and depth, respectively, show the pre- and after-shock locations during about two years (05 Jan. 2018 to 30 Dec. 2019). S1-5 are the fault segments. P1-7 show the locations of the slip profiles from InSAR data in (b). (b) The cross-section profiles of P1-7 along the 2018 Palu rupture

125 **show the N-S slip amount along the segments S1-5. Arrows indicate the position of the rupture (also in (c)). (c) The secondary rupture (white line) is shown with the main rupture (red line). (d) The vertical deformation from the InSAR data is illustrated. The arrows show the horizontal displacements, and the colored dots show the vertical deformation.**

Thus, both InSAR and seismic data indicate that the Palu event is a multi-segmented rupture. To understand the geometry and

130 mechanism of such a segmented strike-slip event under such tectonic settings requires simulating the fault's historic

deformation and coseismic ruptures.

4 Simulated the fault rupture using DEM

To model the 3D geometry of the coseismic rupture plane and the deformation of surrounding zones, particularly the fault pattern of propagation from depth to surface, we implemented the discrete element method (DEM), detailed below.

135 ### 4.1 Methodology and procedure of DEM

The mechanical behavior of the seismogenic crust is approximated as initially modeled by previous studies (e.g., Cundall and Strack, 1979; Donzé et al., 1996; Donzé et al., 1994). The material is represented as an assembly of particles interacting according to predefined laws. The motion of that material's constitutive particles governs its overall behavior (ruled by Newton's second law).

140 The computing cycle can be decomposed into four main steps related respectively to (1) the determination of the position of the constitutive elements, (2) the determination of their potential interaction, (3) the computation of the forces applied to each of them according to predefined interaction laws, and (4) the calculation of their updated positions through the integration of the equations of motion. The calculation cycle is repeated iteratively until the simulation stops.

Because of the dynamic formulation of the method (explicit time domain integration), a non-viscous damping is used to
145 dissipate kinetic energy and facilitate convergence toward quasi-static equilibrium. This damping directly acts on the forces—torques, respectively—in the equations of motion, so the displacements are calculated from the damped force. This is a convenient numerical tool to ensure the quasi-staticity of the simulations (see Duriez et al., 2016, for details). The behavior of the simulated medium is controlled by the behavior defined at the inter-particle scale. The inter-particle behavior of our DEM model can be decomposed into the normal and tangential directions of the contact plane. The normal contact model accounts
150 for both divergence and convergence (Fig. 3).
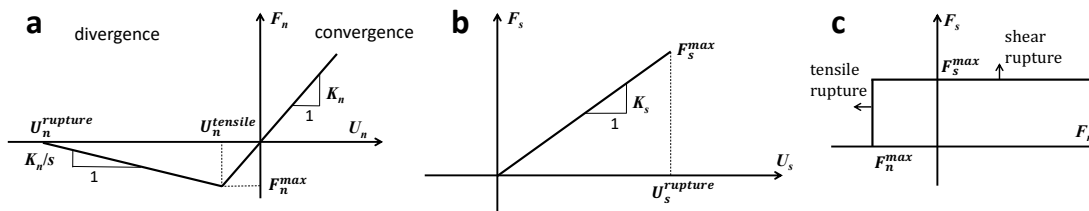
Figure 3: Contact model used in the simulations with (a) normal behavior; (b) tangential behavior; and (c) the micro failure envelope.

155

In the convergence regime (compression of the contact/bond), the normal force F_n is computed as:

$$F_n = K_n \cdot U_n \,,$$

where U_n is the normal component of the relative displacement between particles A and B, and K_n is the normal stiffness derived from the properties assigned to the particles, represented as:

$$K_n = \frac{2 \cdot E_A \cdot R_A \cdot E_B \cdot R_B}{E_A \cdot R_A + E_B \cdot R_B} \,,$$

where R_A and R_B are the radii of the particles, and E_A and E_B are their respective elastic moduli directly related to the bulk
160   modulus of the simulated medium.

In a divergence regime (extension of the contact/bond), the normal force is computed with the same stiffness as that in the convergence regime. The inter-particle distance can increase up to $U_n^{tensile}$ for which the maximum admissible tensile force F_n^{max} is reached:

$$F_n^{max} = t \cdot A_{int} \,,$$

with t the tensile strength of the interparticle bond and $A_{int} = \pi \cdot (\min{(R_A, R_B)})^2$ the interacting surface area between A and
165   B. When F_n^{max} is reached, the force is not set to zero immediately as is usually the case in brittle rock modeling (Scholtès and Donzé, 2013). Instead, F_n gradually decreases, following the softening behavior at the particle scale, between $U_n^{tensile} < U_n < U_n^{rupture}$, according to:

$$F_n = F_n^{max} - \frac{K_n}{s}(U_n - U_n^{tensile}),$$

where s is a weakening coefficient that needs to be defined. If the inter-particle distance continues to increase, the inter-particle bond breaks when $U_n > U_n^{rupture}$ and all forces are set to zero. A crack is then defined at the location of the bond breakage.

170   As in classic DEM formulations (Hart et al., 1988), the tangential force $F_s^{(t)}$ at the current time step t is computed incrementally as:

$$F_s^{(t)} = F_s^{(t-\Delta t)} + K_s \cdot \Delta U_s \,,$$

where $F_s^{(t-\Delta t)}$ is the force computed at the previous time step; ΔU_s is the incremental tangential displacement between A and B, and K_s is the tangential stiffness, defined as $K_S = a \cdot K_n$ with a, a coefficient related to the Poisson's ratio of the simulated medium.

175   As for the normal force, a maximum admissible tangential force, F_s^{max}, is defined as:

$$F_s^{max} = c \cdot A_{int} \,,$$

where c is the inter-particle cohesion (Fig. 3). Once the tangential force reaches this limit, the inter-particle bond breaks, and the forces are set to zero. A crack is then defined at the location of the bond breakage.

One additional parameter is introduced to enable healing of newly created inter-particle contacts. Bonds are thus created when new inter-particle contacts are detected during the simulation. These bonds have the same strength as the initial ones. This is
180   a way to model the healing processes that take place along faults. It permits controlling the dilatancy of the medium undergoing failure. For the tectonic deformation, either the fault rupture modeling or observations after the big seismic event suggest a fast-healing process of the fault zone on the order of decades or even shorter (Gratier et al., 2003; Renard et al., 2000; Xue et al., 2013). Thus, we considered the rapid healing processes in our modeling.

4.2 Modeled rupture geometry, slip dislocation, and recurrence period

Testing the impact of rupture complexity on a seismic hazard assessment requires understanding the mechanism of segmentary faulting behavior. Here, we took the 2018 Palu rupture as an example. We derived the fault geometry from the surface observations to propose a dynamic model through DEM (Fig. 4) and parameter settings (Table 1). To set up an initial model condition for the fault trace, we referred to the fault geometry of the Palu rupture and simplified it as a plane at depth (black
190   dashed line in Fig. 1b). We simulated the development of the fault from a depth of ca. 15 km (Fig. 4), corresponding to the slip dislocation model of this event (Socquet et al., 2019). We decided the size of the fault, in particular the pre-existing segments, based on the historic ruptures. Based on the previous ruptures in 2009 and 1909, we set the pre-existing fault at the southern tip of the 2018 Palu rupture (near P4) with weak strength (Table 1) along the fault plane by those two events (the 2009 Palu segment and 1909 Saluki segment events in Fig. 1). At the depth, the 10°-curved basement fault alignment (Fig. 4c)
195   is consistent with both the tectonic loading in this region (Socquet et al., 2006) and the deep slip model (Scholz, 2002).

Table 1. Parameters for modeling

Parameter	Symbol	Value	Unit
Number of elements	-	200,000	-
Mean element radius	R	4	[m]
Ratio of largest to smallest element	-	1.86	[-]
Interaction range coefficient	γ_{int}	1.15	[-]
Particles' elastic modulus	E	1	[MPa]
Tangential stiffness coefficient	a	0.008	[-]
Tensile strength of model	t	1	[kPa]
Cohesion of model	c	1	[kPa]

Weakening coefficient	s	70	[-]
Shortening rate of indenter	v	2.5	[m/s]
Damping coefficient	D_a	0.4	[-]
Time interval coefficient	-	0.4	[-]
Gravitational acceleration	g	0.08	[m/s^2]
Tensile strength of pre-existing fault	t	0.2	[kPa]
Cohesion of pre-existing fault	c	0.2	[kPa]
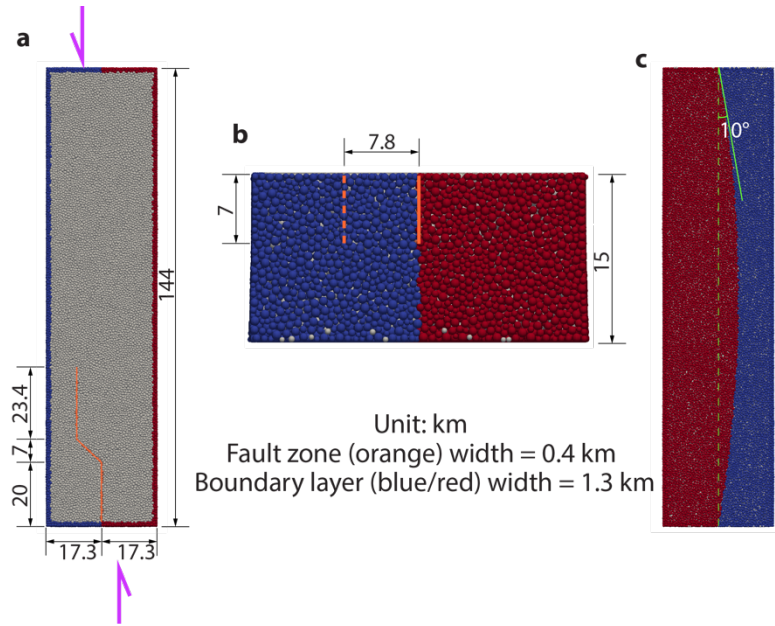
Figure 4: Model setup with 200,000 spherical elements: (a) the top view of the model; (b) the view from the south; and (c) the bottom view of the model. The loading boundaries are in red and blue. The deformation model is in grey. The pre-existing fault is in orange. The two purple half-arrows show the loading direction: the red boundary moves to the north, and the blue boundary moves to the south. The dimensions of the model and the pre-existing fault are as shown: the model is 144 km long, 34.6 km wide and 15 km deep; the pre-existing fault is ca. 7.0 km deep and ca. 50.4 km long with one step-over from the south end. The curved loading boundary at the bottom is 10° convex to the west.

To simulate the behavior of the continental crust and rupture deformation using the proposed approach, the model needed to be calibrated (Fig. 5). The calibration procedure of DEM models consists of adjusting the set of interparticle parameters so the emergent macroscopic behavior is representative of the targeted medium. To determine the relevant set of interparticle parameters for the crust, we ran a series of triaxial compression test simulations on a sample of the crust assembly under

different confining pressures (Fig. 5a). We considered confining pressures varying from 0 to 400 MPa to represent the depths of the crust (Fig. 5b). Following the calibration procedure proposed by Scholtès and Donzé (2013), we set the interparticle parameters presented in Table 1, which produces the macroscopic mechanical behavior presented in Fig. 5. The stress-strain curves of the crustal rock with different depths show the rock strength increasing with the depth. Since the healing process is

215   considered in the model, the strain-softening behavior along the curves presents with different pressures, but with the degree of strain-softening decreasing with the different pressures. The failure envelope line (Fig. 5c) shows the stress increasing approximately lineally with the lateral pressure, which is similar to the Mohr-Coulomb criterion. After the calibration, we could use the parameter settings and the model to simulate the tectonic deformation and rupture behavior.

220
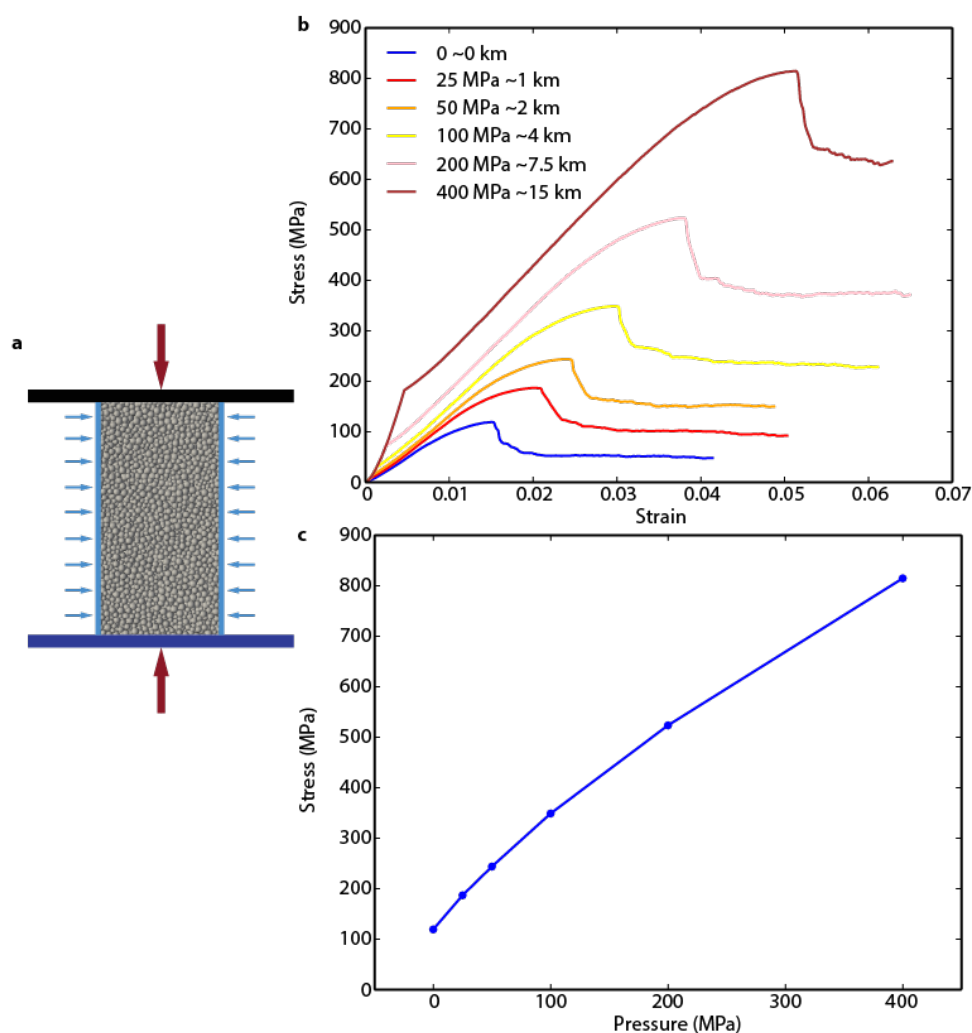
Figure 5: Triaxial compression test simulations performed on the calibrated model (see Table 1): (a) the setup, (b) the

stress-strain responses obtained for different confining pressures corresponding to different depths up to ca. 15 km (400 MPa); and (c) the relationship between the compressive strength of the simulated crust and the confining pressure (failure envelope).

225

In the simulation, we recorded each time the boundary slipped 2 m during the modelled deformation, which represents a period of ca. 50 years in nature. In the first stage, ruptures concentrate along the Palu and Saluki segments of the Palu-Koro faults (Steps 0-90 in Fig. 6), corresponding to the locations of the events in 2009 and 1909. Note that we did not consider rupture events in other segments along the Palu-Koro fault or the Matano fault. Afterward, an en echelon pattern started developing

230 along the northern part of the Palu rupture (Steps 90-100 and Steps 100-110 in Fig. 6), corresponding to an unidentified fault zone before the 2018 Palu event. In this stage, the fault has not yet matured. In the second stage (Steps 110-120 in Fig. 6), cracks distribute almost homogenously along the entire Palu rupture, particularly along its northern part, which was unmatured before. Thus, in this period, the fault becomes mature, resulting in a ca. 140 km-long rupture, corresponding to an event like the 2018 one. During the further loading period (Steps 120-180 in Fig. 6), cracks or events occur repeatedly along the entire

235 mature fault, illustrating the spatial and temporal distribution of seismicity along this fault system. Events like the 2018 one would reoccur persistently in the future.
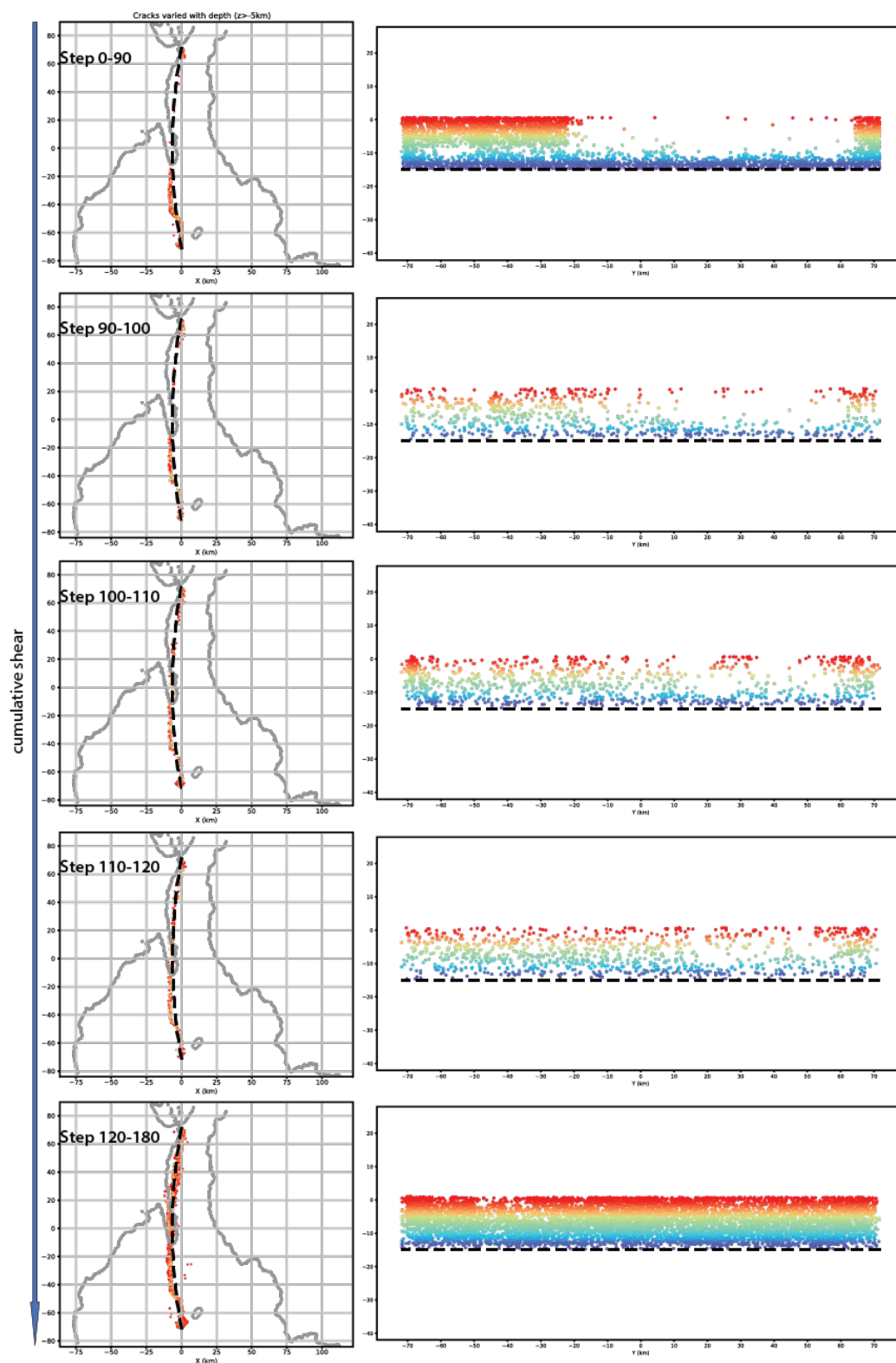
Figure 6: Numerical model result sequences: each step has a ca. 2 m movement along the model. At Steps 0-90, corresponding to ca. 4,500 years, the cumulative cracks occurred along the pre-existing segments from depth to the surface, while along the unidentified fault zone, cracks happened only at the creeping depth; they had not yet propagated to the shallow part. At Steps 90 to 100, corresponding to ca. 500 years, very few cracks occurred on the surface. During this period, it seems impossible to coalesce them from the bottom to the surface together to form the entire rupture. At Steps 100 to 110, corresponding to ca. 500 years, more cracks take place along the north segments (representing unidentified segments) than the previous stages, but still with significant gaps between segments on the surface. This suggests that the rupture still might not be coalesced to form the entire rupture. At Steps 110 to 120, corresponding to ca. 500 years, the cracks seem distributed along the entire fault. Since this period could allow the segments to connect the pre-existing fault in the south and unmapped faults in the north together and change the entire fault from immature to mature, the 2018 Palu rupture event probably occurs during this period. At Steps 120 to 180, corresponding to ca. 3,000 years, cracks homogenously distribute along the entire fault plane, inferring that further events repeatedly occur along the entire fault system.

In the period of Steps 110-120, both the deformation on the surface and the crack distributions along the fault plane suggest the fault has been ruptured entirely during the coseismic period of the 2018 Palu event. Thus, we detail the DEM at these steps in the forms of surface deformation and rupture patches (Fig. 7). The models show the slips at profiles L1 to L5 are 3.3, 1.0, 3.0, 6.0, and 3.5 m, respectively (Fig. 7b). The slip pattern (peak in the central segment) and the level of the peak slip (with slip of ca. 6.0 m) are consistent with the InSAR observations in the 2018 Palu event (Fig. 2). On the surface (with a depth <5 km), our model presented a total of 6 segments, F1 to F6 (Fig. 8a), to fit the patterns of the crack swarms (red and orange dots). At depth, the crack distribution confirms that a total of 6 sub-fault planes are vertically wrenched from north to south (Fig. 8a) form the entire fault geometry of the event, which ruptures the fault from immature (unmapped) to mature (mapped). The maturity of the fault (the 2018 Palu rupture zone) is also affected by the pre-existing fault segments (the Palu and Saluki segments of the Palu-Koro Fault). We could identify the dip direction of each sub-fault that dips almost vertically with slightly horizontal components (Figs. 8a and b). The segments in the two ends (F1 and F6) dip to the west, whereas the central segments (F3 to F5) dip to the east, and F2 is almost vertical with a slight horizontal component. The modeled dipping pattern is in good agreement with the InSAR observations of the Palu event (Fig. 2). Note that the dip direction changes from F1 to F6 along the segments are different from the ideal Riedels (Mandl, 2005; Naylor et al., 1986; Lefevre et al., 2020; Jiao et al., 2021). The southern parts, including F5 and F6, are dominantly affected by the mature fault (mapped fault). Thus, the maturity of the fault affects the fault segments.
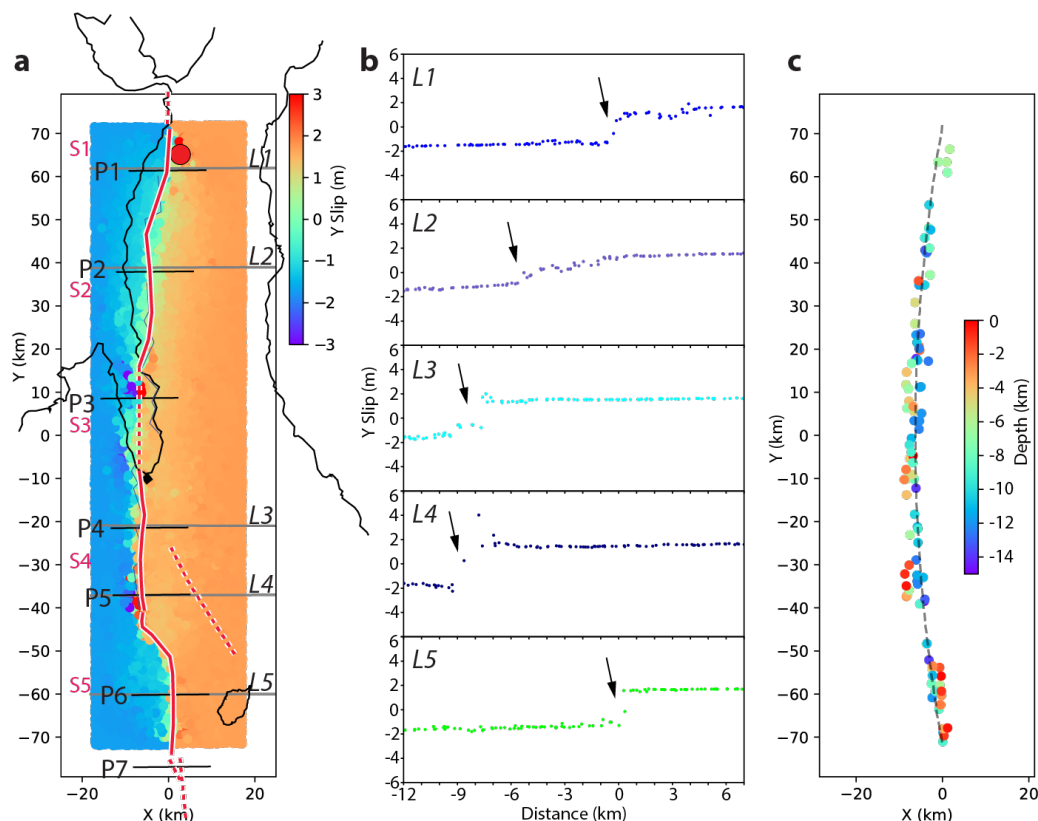
Figure 7: Illustration of the deformation and crack distribution of the moment that could be comparable to the 2018 Palu event: (a) The modeling movement distribution along the N-S direction during one event is shown by colored dots. The larger red dot shows the epicenter of the 2018 Palu event. The profile lines L1-L5 show the locations of the profiles in (b). The coastal line, profile lines P1-P5, segments S1-S5, surface rupture of the 2018 Palu event (red line with white background), and secondary rupture (thin blue line in the back) are from Fig. 2c. (b) Slips in the N-S component are along profiles L1-L5: black arrows indicate the rupture locations in the model. (c) In the modeled crack location during the event, the dashed curve shows the boundary of the N-S loading plates at the depth.

5 Discussion and Conclusions

5.1 Modeled rupture on the complex fault plane

In this study, we examined the fault geometry complexity during segmented rupture seismic events and further to quantify the seismic hazard. We propose a dynamic model to illustrate behaviors of the earthquakes with complex rupture patterns using the case of the 2018 Palu event. Our DEM model could illustrate the spatial and temporal distribution along the entire fault system, including the immature segments in the north and mature segments in the south. The simulations showed that before

285   the big event, there are few frequent seismic activities with smaller slip patches (corresponding to smaller magnitudes) in the southern segments, corresponding to the events, such as the 1909 Saluki segment and 2009 Palu segment events (Fig. 1). Then activities that could rupture the entire fault system follow these small activities, resulting in an event like the 2018 Palu earthquake. This rupture event could propagate along the immature part in the north and mature part in the south together. This model explains the occurrence of a large event like the 2018 event, suggesting coseismic rupture on both immature and mature

290   segments. During the period of this large event, the modeled surface deformation in the forms of slip pattern (peak in the central segment) and level of the peak slip (with slip of ca. 6.0 m) are consistent with the InSAR observations (Fig. 2).

The 2018 Palu event ruptured along several fault segments on the surface with a super-fast rupture speed (also known as *super shear*; Bao et al., 2019; Socquet et al., 2019). It suggests that the single fault at the depth, which could provide the super-fast rupture speed along the fault, and the en echelon pattern on the surface. Both the observation and the model present different

295   dipping directions of each fault segment (Figs. 2 and 8), since the 2018 Palu event and the simulated one ruptured segmentally with alternating dipping directions on segments. Generally, such a segmented en echelon pattern could be explained by the theory of a wrenched sub-fault plane distributed along a strike-slip fault system (e.g., Naylor et al., 1986). This theory concluded that the formation of the Anderson-type wrench faults is accounted for in Coulomb-Mohr's theory with tectonic loading. Considering the orientations of the potential slips associated with the principal stress directions at different levels of

300   the inner wrench zone, the synthetic wrench faults fit into the slip pattern and merge with the basement fault. Each synthetic Riedel shear has a helicoidal shape (Lefevre et al., 2020; Mandl, 2005). The synthetic Riedel shears diverge from the basement fault with decreasing distance from the basement fault. Thus, the wrenched fault system is the single simple and smooth shear fault at depth. With its development, the shear fault twists and segmentally propagates to the surface, and then it shows en echelon Riedel shears (sub-faults) with a sense of motion synthetic with the general shear direction (Asaoka et al., 2016; Riedel,

305   1929) on the surface, which rides on the single simple shear fault.

Furthermore, the number and dip direction of wrenching fault segments may be affected by several factors, such as depth (Klinger, 2010), tectonic loading (Naylor et al., 1986), and strength of the plate. Our model has confirmed that the maturity of the fault segments also affects the en echelon Riedel pattern. The dip direction along the segments of the mature southern part differs from the segments of unmatured northern part in the modeling. The maturity of the fault segment changes the dip

310   directions of segments, perhaps even segment sizes. In nature, consider the coseismic slip along the wrench faults of the 2018 Palu event as an example. The 2018 Palu rupture in the northern part includes several immature en echelon fault segments, and the southern part has pre-existing faults from other fault systems next to this rupture fault. The 3D helicoidal shape of the Riedel shear segments from depth to surface is obtained from the modeled rupture of the 2018 Palu event (Fig. 8), obviously distorted by the maturity of fault segments.

315
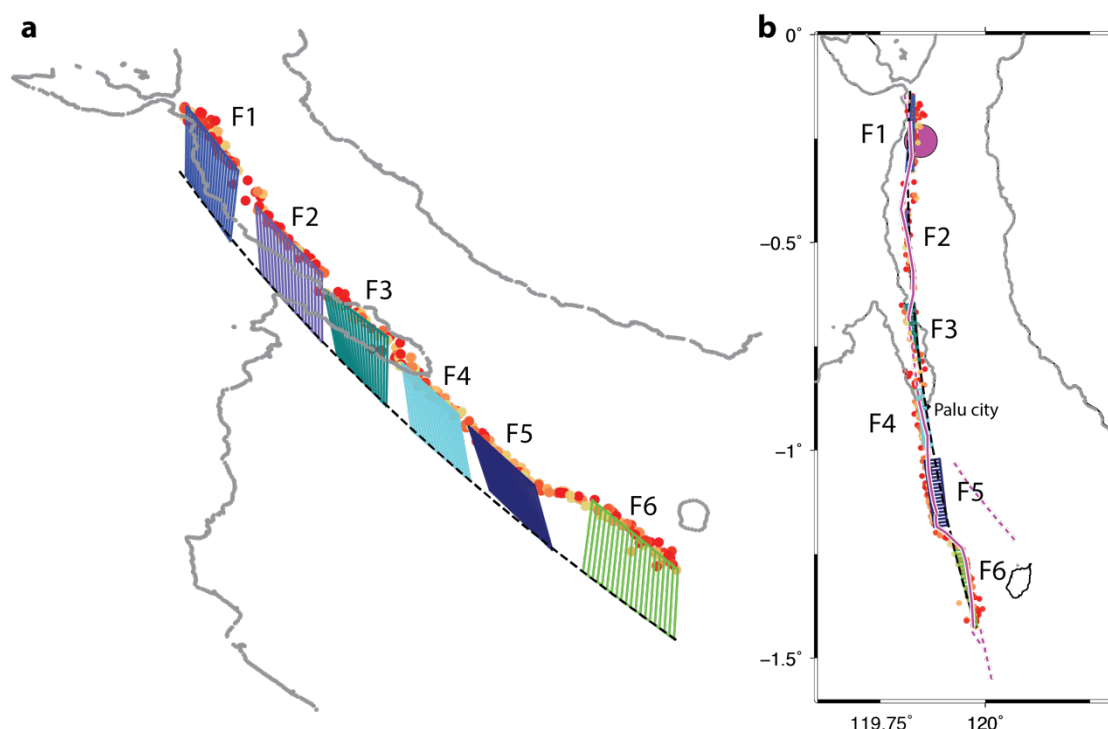
Figure 8: Comparison of the modeling rupture planes with observations of the Palu event: (a) A 3D view of the implied six sub-fault segment planes F1-F6 and the surface cracks (<5 km; in orange and red dots) in the model is shown. The colors of the dots correspond to the crack depth, the same as those shown in Fig. 7c. (b) The map view of the sub-fault planes in (a) and the observed main rupture of the 2018 Palu event (purple line with white background) are shown from Fig. 2a; the big purple dot indicates the location of the 2018 Palu event.

5.2 Application to probabilistic seismic hazard assessment

A probabilistic seismic hazard assessment (PSHA; Cornell, 1968) determines the probability of exceedance of various levels of ground motion over a specified period. Since this assessment quantifies a seismic hazard into a probability, it serves as a key reference in mitigating seismic risk, developing building code legislation, selecting sites for public and private infrastructure, and calculating insurance premiums. Some PSHAs assume an earthquake takes place on a single active fault and that faults (or segments of a fault) are independent of each other. With the 2017 national seismic hazard maps of Indonesia (Irsyam et al., 2020) as an example, the hazard was contributed from each fault segment with maximum magnitude. The 2018 M_w7.5 Palu rupture can be associated with the Palu, Saluki, and Moa fault segments with maximum magnitudes of 6.8, 6.9, and 7.1, respectively. The assumption underestimates the maximum magnitude when an earthquake ruptures along several faults or fault segments, however.

Some previous studies (e.g., Chan et al., 2020) have proposed innovative approaches that assumed an earthquake could rupture along multiple fault segments. Our approach replies on identification of potential faults/segments that would rupture

335   coseismically. In this study, we demonstrated that our model could illustrate spatial and temporal distribution along the entire fault system to quantify the possibility of earthquake occurrence as a function of magnitude (based on the rupture size). We are aware that implemented parameters (Table 1) would drive the outcomes of the DEM model. Variations of each parameter could be regarded as epistemic uncertainties and be assumed into a logic tree in a PSHA.

Acknowledgements

340   This study was supported by the Ministry of Science and Technology in Taiwan—under the grants MOST 109-2116-M-008 -029 -MY3, MOST 110-2124-M-002 -008008, and MOST 110-2634-F-008-008. This work is financially supported by the Earthquake Disaster & Risk Evaluation and Management Center (E-DREaM) from the Featured Areas Research Center Program within the framework of the Higher Education Sprout Project by the Ministry of Education in Taiwan. We thank Prof. Ares Rosakis for discussion about the conditions of super-shear rupture.

345   **Author contribution**

LJ performed the synthetic analyses of the Palu earthquake rupture deformation and conducted the numerical modeling. TW and GF provided the InSAR data analysis of the surface deformation from the 2018 earthquake. PT provided the geological analysis. CHC and LJ wrote the manuscript and administrated the project. All authors contributed to scientific discussion, critical validation of results, and writing the manuscript.

350   **Competing interests**

The authors declare they have no conflict of interest.

References

Asaoka, A., Sawada, Y., Yamada, S., 2016. Riedel shear band formation with flower structures that develop at the surface ground on a strike slip fault. Japanese Geotechnical Society Special Publication 2, 751-754.

355   Bacques, G., de Michele, M., Foumelis, M., Raucoules, D., Lemoine, A., Briole, P., 2020. Sentinel optical and SAR data highlights multi-segment faulting during the 2018 Palu-Sulawesi earthquake (Mw 7.5). Sci Rep 10, 9103.

Bao, H., Ampuero, J.-P., Meng, L., Fielding, E.J., Liang, C., Milliner, C.W.D., Feng, T., Huang, H., 2019. Early and persistent supershear rupture of the 2018 magnitude 7.5 Palu earthquake. Nature Geoscience.

Broberg, K.B., 1999. Cracks and fracture. Elsevier.

360   Burridge, R., 1973. Admissible speeds for plane-strain self-similar shear cracks with friction but lacking cohesion. Geophysical Journal of the Royal Astronomical Society 35, 439-455.

Chan, C. H., Ma, K. F., Shyu, J. B. H., Lee, Y. T., Wang, Y. J., Gao, J. C., ... & Rau, R. J. (2020). Probabilistic seismic hazard assessment for Taiwan: TEM PSHA2020. Earthquake Spectra, 36(1_suppl), 137-159.

Chang, C. C., Chang, C. Y., & Chan, C. H. (2022). Quantifying the probability and uncertainty of multiple-structure rupture
365   and recurrence intervals in Taiwan. Natural Hazards and Earth System Sciences Discussions, 1-22.

Cornell, C. A., 1968. Engineering seismic risk analysis. Bulletin of the seismological society of America, 58(5), 1583-1606.

Cundall, P.A., Strack, O.D.L., 1979. Discrete numerical model for granular assemblies. Geotechnique 29, 47-65.

Daryono, M.R., 2016. Paleoseismologi tropis Indonesia. Thesis of Institut Teknologi Bendung

Donzé, F., Magnier, S.A., Bouchez, J., 1996. Numerical modeling of a highly explosive source in an elastic-brittle rock mass.
370   Journal of Geophysical Research-Solid Earth 101, 3103-3112.

Donzé, F., Mora, P., Magnier, S.A., 1994. Numerial Simulation of Faults and Shear Zones. Geophysical Journal International 116, 46-52.

Dreger, D.S., Oglesby, D.D., Harris, R., Ratchkovski, N., Hansen, R., 2004. Kinematic and dynamic rupture models of the November 3, 2002 Mw7. 9 Denali, Alaska, earthquake. Geophysical research letters 31.

375   Duriez, J., Scholtès, L., Donzé, F.-V., 2016. Micromechanics of wing crack propagation for different flaw properties. Engineering Fracture Mechanics 153, 378-398.

Fang, J., Xu, C., Wen, Y., Wang, S., Xu, G., Zhao, Y., Yi, L., 2019. The 2018 Mw 7.5 Palu earthquake: A supershear rupture event constrained by InSAR and broadband regional seismograms. Remote Sensing 11, 1330.

Fukuyama, E., Olsen, K.B., 2002. A condition for super-shear rupture propagation in a heterogeneous stress field. Pure Appl.
380   Geophys. 159, 2047-2056.

Gratier, J.P., Favreau, P., Renard, F., 2003. Modeling fluid transfer along California faults when integrating pressure solution crack sealing and compaction processes. Journal of Geophysical Research: Solid Earth 108.

Hamling, I. J., Hreinsdóttir, S., Clark, K., Elliott, J., Liang, C., Fielding, E., ... & Stirling, M., 2017. Complex multifault rupture during the 2016 M w 7.8 Kaikōura earthquake, New Zealand. Science, 356(6334), eaam7194.

385   Hart, R., Cundall, P., Lemos, J., 1988. Formulation of a three-dimensional distinct element model—Part II. Mechanical calculations for motion and interaction of a system composed of many polyhedral blocks, International Journal of Rock Mechanics and Mining Sciences & Geomechanics Abstracts. Elsevier, pp. 117-125.

Irsyam, M., Cummins, P. R., Asrurifak, M., Faizal, L., Natawidjaja, D. H., Widiyantoro, S., ... & Syahbana, A. J. (2020). Development of the 2017 national seismic hazard maps of Indonesia. Earthquake Spectra, 36(1_suppl), 112-136.

390   Jiao, L., Klinger, Y., Scholtes, L., 2021. Fault segmentation pattern controlled by thickness of brittle crust. Geophysical Research Letters 48, e2021GL093390.

Klinger, Y., 2010. Relation between continental strike-slip earthquake segmentation and thickness of the crust. Journal of Geophysical Research: Solid Earth 115.

Klinger, Y., Xu, X., Tapponnier, P., Van der Woerd, J., Lasserre, C., King, G., 2005. High-resolution satellite imagery mapping
395   of the surface rupture and slip distribution of the M w~ 7.8, 14 November 2001 Kokoxili earthquake, Kunlun fault, northern Tibet, China. Bulletin of the Seismological Society of America 95, 1970-1987.

Lefevre, M., Souloumiac, P., Cubas, N., Klinger, Y., 2020. Experimental evidence for crustal control over seismic fault segmentation. Geology.

Mandl, G., 2005. Rock joints. Springer.

400   Manighetti, I., Campillo, M., Bouley, S., Cotton, F., 2007. Earthquake scaling, fault segmentation, and structural maturity. Earth Planet. Sci. Lett. 253, 429-438.

Naylor, M., Mandl, G.t., Supesteijn, C., 1986. Fault geometries in basement-induced wrench faulting under different initial stress states. Journal of Structural Geology 8, 737-752.

Natawidjaja, D.H., Daryono, M.R., Prasetya, G., Liu, P.L., Hananto, N.D., Kongko, W., Triyoso, W., Puji, A.R., Meilano, I.,
405   Gunawan, E., 2021. The 2018 M w7. 5 Palu 'supershear'earthquake ruptures geological fault's multisegment separated by large bends: results from integrating field measurements, LiDAR, swath bathymetry and seismic-reflection data. Geophysical Journal International 224, 985-1002.

Okuwaki, R., Hirano, S., Yagi, Y., Shimizu, K., 2020. Inchworm-like source evolution through a geometrically complex fault fueled persistent supershear rupture during the 2018 Palu Indonesia earthquake. Earth Planet. Sci. Lett. 547, 116449.

410   Oral, E., Weng, H., Ampuero, J.P., 2020. Does a damaged-fault zone mitigate the near-field impact of supershear earthquakes?—Application to the 2018 7.5 Palu, Indonesia, earthquake. Geophysical Research Letters 47, e2019GL085649.

Perrin, C., Manighetti, I., Ampuero, J.P., Cappa, F., Gaudemer, Y., 2016. Location of largest earthquake slip and fast rupture controlled by along-strike change in fault structural maturity due to fault growth. Journal of Geophysical Research: Solid Earth 121, 3666-3685.

415   Petersen, M. D., Dawson, T. E., Chen, R., Cao, T., Wills, C. J., Schwartz, D. P., and Frankel, A. D., 2011. Fault displacement hazard for strike-slip faults. Bull. Seism. Soc. Am. 101 805-825.

Renard, F., Gratier, J.-P., Jamtveit, B., 2000. Kinetics of crack-sealing, intergranular pressure solution, and compaction around active faults. Journal of Structural Geology 22, 1395-1407.

Riedel, W., 1929. Zur Mechanik Geologischer Brucherscheinungen. Zentral-blatt fur Mineralogie, Geologie und Paleontologie
420   1929B, 354–368.

Rubino, V., Rosakis, A., Lapusta, N., 2017. Understanding dynamic friction through spontaneously evolving laboratory earthquakes. Nature Communications 8, 15991.

Scholtès, L., Donzé, F.V., 2013. A DEM model for soft and hard rocks: Role of grain interlocking on strength. J. Mech. Phys. Solids 61, 352-369.

425   Scholz, C.H., 2002. The mechanics of earthquakes and faulting. Cambridge university press.

Segall, P., Pollard, D., 1980. Mechanics of discontinuous faults. Journal of Geophysical Research: Solid Earth 85, 4337-4350.

Silver, E.A., McCaffrey, R., Smith, R.B., 1983. Collision, rotation, and the initiation of subduction in the evolution of Sulawesi, Indonesia. Journal of Geophysical Research: Solid Earth 88, 9407-9418.

Šmilauer, V., 2010. Cohesive particle model using the discrete element method on the yade platform. PhD thesis at Czech Technical University in Prague, Faculty of Civil Engineering & Université Grenoble I – Joseph Fourier, École doctorale I-MEP2.

Socquet, A., Hollingsworth, J., Pathier, E., Bouchon, M., 2019. Evidence of supershear during the 2018 magnitude 7.5 Palu earthquake from space geodesy. Nature Geoscience.

Socquet, A., Simons, W., Vigny, C., McCaffrey, R., Subarya, C., Sarsito, D., Ambrosius, B., Spakman, W., 2006. Microblock rotations and fault coupling in SE Asia triple junction (Sulawesi, Indonesia) from GPS and earthquake slip vector data. Journal of Geophysical Research: Solid Earth 111.

Takao, M., Tsuchiyama, J., Annaka, T., and Kurita, T., 2013. Application of probabilistic fault displacement hazard analysis in Japan. Journal of Japan Association for Earthquake Engineering 13 17-32.

Ulrich, T., Vater, S., Madden, E.H., Behrens, J., van Dinther, Y., van Zelst, I., Fielding, E.J., Liang, C., Gabriel, A.-A., 2019. Coupled, Physics-based Modeling Reveals Earthquake Displacements are Critical to the 2018 Palu, Sulawesi Tsunami.

Watkinson, I.M., Hall, R., 2017. Fault systems of the eastern Indonesian triple junction: evaluation of Quaternary activity and implications for seismic hazards. Geological Society, London, Special Publications 441, 71-120.

Wesnousky, S.G., 2006. Predicting the endpoints of earthquake ruptures. Nature 444, 358.

Wesnousky, S.G., 2008. Displacement and geometrical characteristics of earthquake surface ruptures: Issues and implications for seismic-hazard analysis and the process of earthquake rupture. Bulletin of the Seismological Society of America 98, 1609-1632.

Xu, X., Chen, W., Ma, W., Yu, G., Chen, G., 2002. Surface rupture of the Kunlunshan earthquake (Ms 8.1), northern Tibetan plateau, China. Seismological Research Letters 73, 884-892.

Xue, L., Li, H.-B., Brodsky, E.E., Xu, Z.-Q., Kano, Y., Wang, H., Mori, J.J., Si, J.-L., Pei, J.-L., Zhang, W., 2013. Continuous permeability measurements record healing inside the Wenchuan earthquake fault zone. Science 340, 1555-1559.

Youngs, R. R., Arabasz, W. J., Anderson, R. E., Ramelli, A. R., Ake, J. P., Slemmons, D. B., ... and Rogers, A. M., 2003. A methodology for probabilistic fault displacement hazard analysis (PFDHA). Earthquake spectra 19 191-219.